Supplementary Information (SI) for Nanoscale.

Supplementary Information

Two-Dimensional Mn_2CF_2 MXene-Based Magnetic Tunnel Junctions with Giant Spin Filter Tunnel Magnetoresistance

Sonali S. Pradhan[1], G. Vaitheeswaran[2,*] and V. Kanchana[1,*]

[1] *Department of Physics, Indian Institute of Technology Hyderabad, Kandi – 502285, Sangareddy, Telangana, India.*

[2] *School of Physics, University of Hyderabad, Prof. C. R. Rao Road, Gachibowli, Hyderabad 500046, Telangana, India.*

Email: kanchana@phy.iith.ac.in; ph23resch01015@iith.ac.in; vaithee@uohyd.ac.in

1 AIMD

Ab initio molecular dynamics (AIMD) simulations were performed in the NVT ensemble using a $2 \times 2 \times 1$ supercell to examine the thermal stability of the Mn_2CF_2 monolayer and the Mn_2CF_2/MoS_2 heterostructures. The calculations were conducted at 300 K for a total simulation time of 5000 fs. As shown in Fig. S1, the temperature fluctuates only slightly around the target value, indicating proper thermal equilibration. Throughout the entire simulation period, the structures retained their stability, and no bond breaking was detected at the end of the calculations.

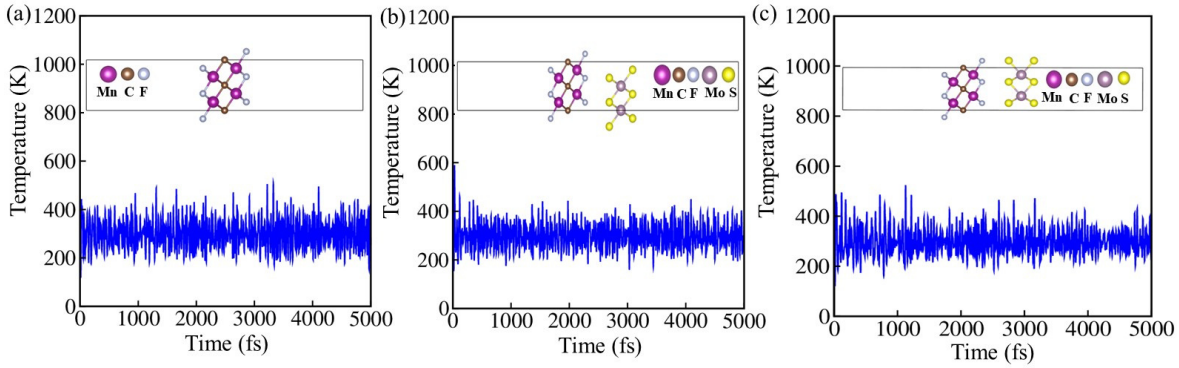

Figure S1: Ab initio molecular dynamics (AIMD) simulations of (a) monolayer Mn_2CF_2 and (b) Mn_2CF_2/1T-MoS_2, and (c) Mn_2CF_2/2H-MoS_2 heterostructure at $T = 300$ K.

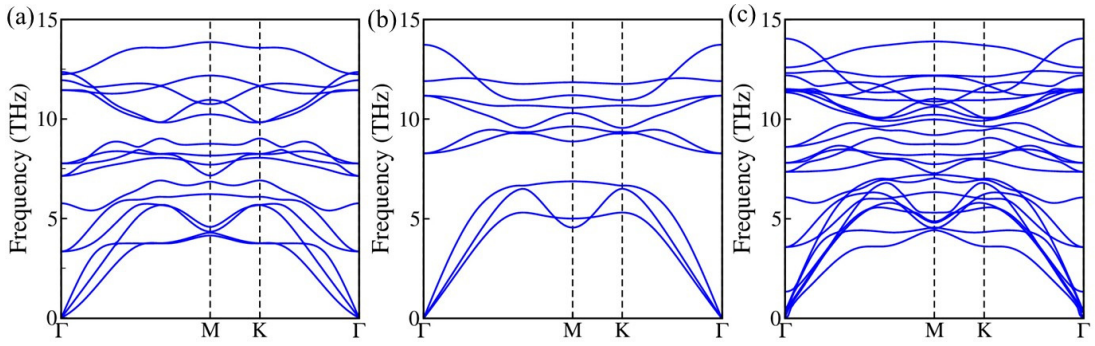

Figure S2: Phonon dispersion of (a) Mn_2CF_2 monolayer, (b) MoS_2 monolayer, and (c) Mn_2CF_2/ MoS_2 heterostructure.

2 Phonon dispersion plots

The phonon dispersion calculations were performed using density functional perturbation theory (DFPT) as implemented in VASP, in conjunction with the Phonopy package, employing a $2 \times 2 \times 1$ supercell. The calculated phonon spectra are presented in Fig. S2. As shown in Fig. S2, no imaginary (negative) phonon modes are observed throughout

the entire Brillouin zone for either the monolayers or the heterostructure, indicating their dynamical stability.

3 DFT+U and HSE06

Upon inclusion of the DFT+U correction, the spin-down bands shift upward, whereas the spin-up bands shift downward. As a result, the half-metallic gap increases with increasing values of the on-site Coulomb parameter U, as shown in Fig. S3.

The band structure calculated using the HSE06 hybrid functional is presented in Fig. S4. The HSE06 results clearly show that the spin-down band gap is larger than that obtained within the DFT+U approach, which is consistent with the well-known tendency of hybrid functionals to provide more accurate band-gap values.

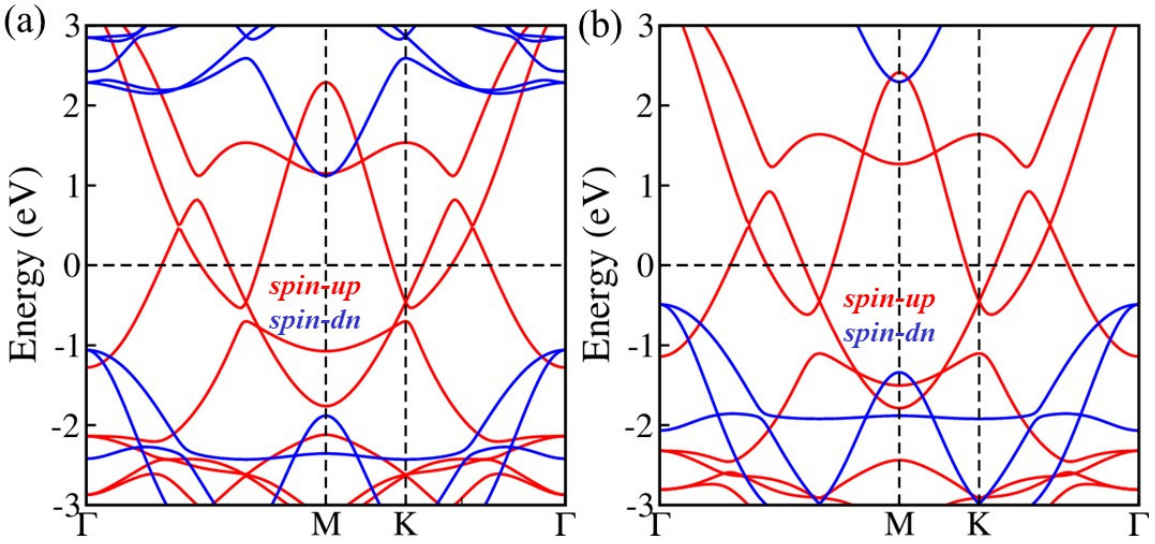

Figure S3: (a) and (b) Spin-polarized band structures of the Mn_2CF_2 monolayer calculated with different Hubbard U values of 3 and 5 eV, respectively, applied to the Mn atoms.

Table S1: Total energies of different FM and AFM configurations for the Mn_2CF_2 monolayer and the Mn_2CF_2/MoS_2 heterostructure. Energies are given in eV, with the lowest-energy configuration set as the reference (0 eV).

Configuration	Mn_2CF_2 (eV)	Mn_2CF_2/MoS_2 (eV)
FM	0.00	0.00
AFM-1	2.30	2.28
AFM-2	1.97	2.03
AFM-3	0.56	0.57

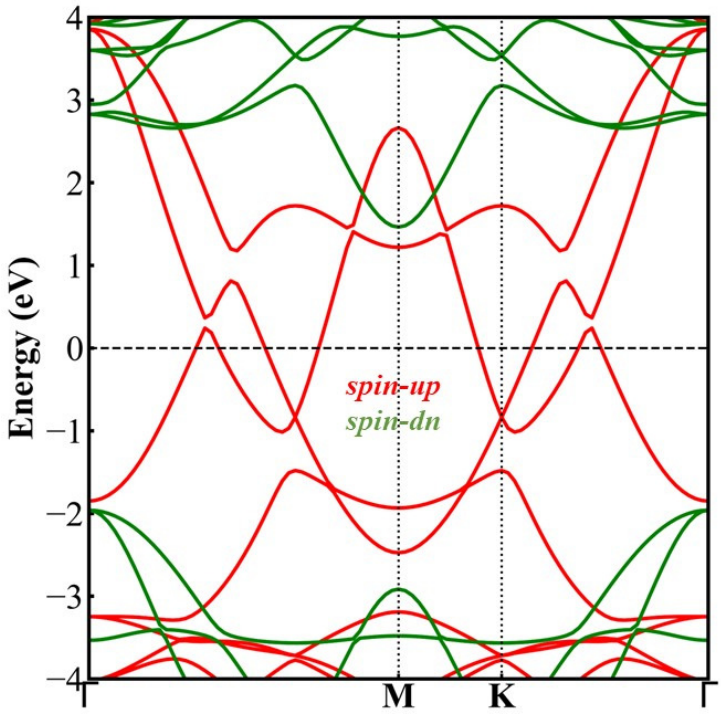

Figure S4: Band structure of the Mn_2CF_2 monolayer calculated using the HSE06 functional.

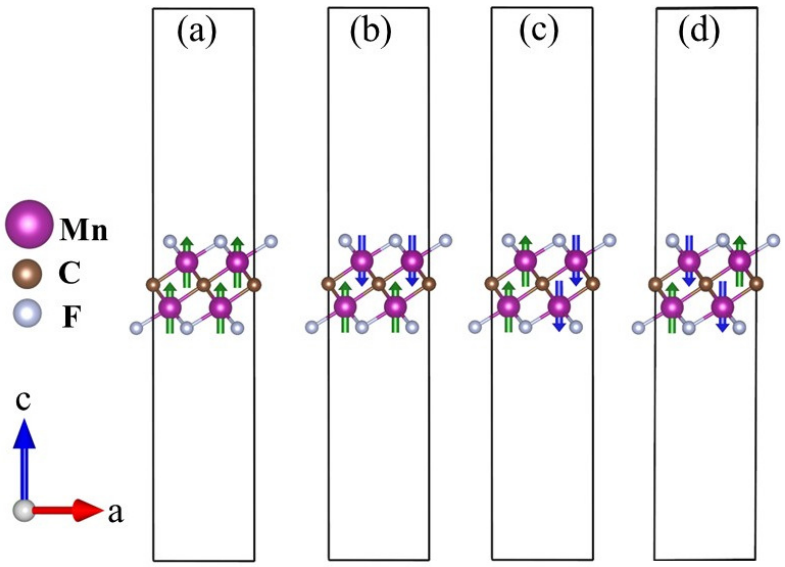

Figure S5: Magnetic configurations for the $2 \times 2 \times 1$ supercell of Mn_2CF_2 monolayer, illustrating the orientations of Mn spins: (a) FM, (b) AFM1, (c) AFM2, and (d) AFM3. Spin-up and spin-down states are shown by green and blue arrows, respectively.

4 Different Stacking Configurations, Interlayer Distance, and Binding Energy

In the Mn_2CF_2/1T–MoS_2 and Mn_2CF_2/2H–MoS_2 van der Waals (vdW) heterostructures, we systematically explored several possible stacking arrangements to identify the most stable interfacial configurations. As illustrated in Fig. S6, each interface exhibits three distinct stacking geometries.

For the Mn_2CF_2/2H-MoS_2 heterostructure Fig. S6(a), in stacking-I, the S atoms of the MoS_2 layer are positioned directly above the bottom F and top Mn atoms of the Mn_2CF_2 layer, while the C atoms are located over the Mo atoms. In stacking-II, the Mo atoms align above the top Mn atoms, the S atoms lie over the top F atoms, and the C atoms occupy bridge sites between adjacent Mo and S atoms. In stacking-III, the Mo atoms are situated above the bottom Mn and top F atoms, whereas the C atoms are positioned nearly above the S sites.

Similarly, for the Mn_2CF_2/1T-MoS_2 heterostructure Fig. S6(b), stacking-I features the bottom S atoms of MoS_2 located above the top F atoms of Mn_2CF_2, with the Mo atoms positioned directly above the C atoms and the Mn atoms occupying the hollow sites of the nearly planar Mo–S network. In stacking-II, the top S atoms are aligned above the top F atoms, the bottom S atoms lie above the C atoms, and the Mo atoms sit atop the upper Mn atoms. In stacking-III, the bottom S atoms are positioned over the bottom F atoms, the Mo atoms reside above the bottom Mn atoms, and the C atoms are located near the hollow positions of the Mo–S hexagon.

Among all configurations considered, stacking-I of both the Mn_2CF_2/1T-MoS_2 and Mn_2CF_2/2H-MoS_2 heterostructures exhibits the lowest binding energy (E_{bind}), indicating that these are the most energetically favorable stacking geometries. Consequently, these two stable stacking-I configurations were selected to construct the vdW MTJs.

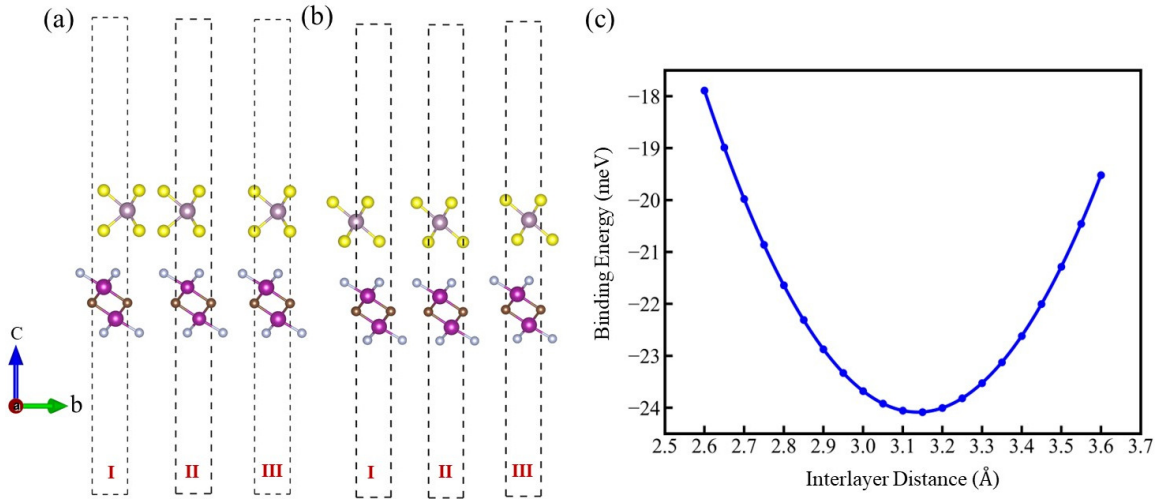

Figure S6: (a) Mn_2CF_2/2H–MoS_2 heterostructure and (b) Mn_2CF_2/1T–MoS_2 heterostructure, showing different stacking configurations; and (c) binding energy as a function of interlayer distance for the Mn_2CF_2/MoS_2 heterostructure.

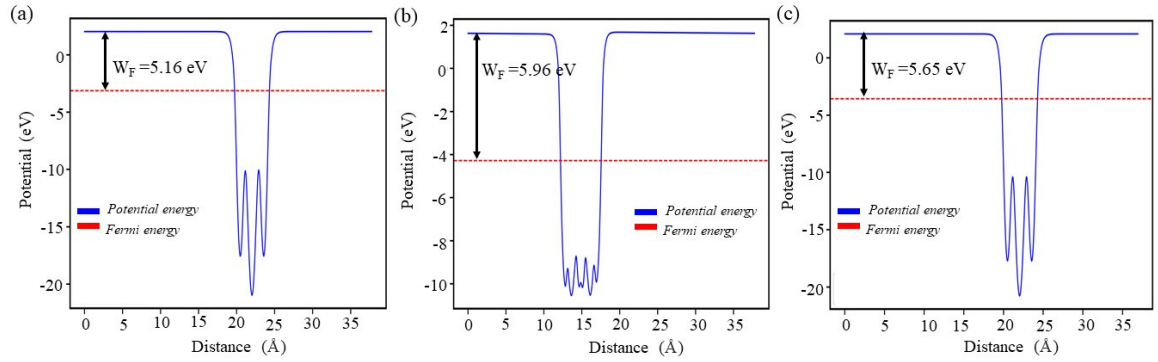

Figure S7: The electrostatic potential E_p for (a) 1T-MoS_2, (b) monolayer Mn_2CF_2, and (c) 2H-MoS_2.

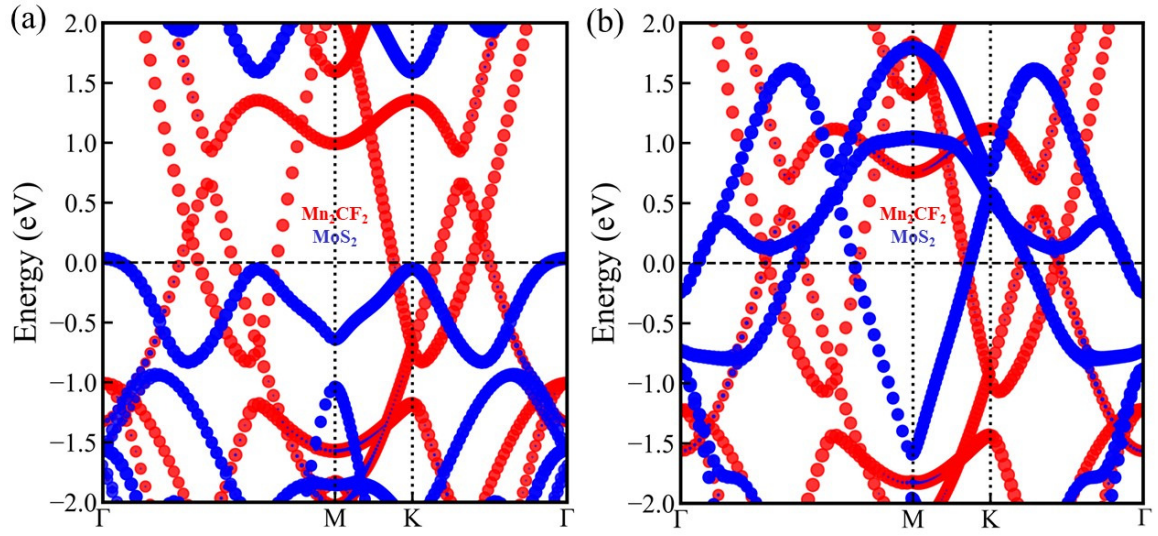

Figure S8: Projected band structures of (a) 2H-MoS_2/Mn_2CF_2 and (b) 1T-MoS_2/Mn_2CF_2 heterostructures.

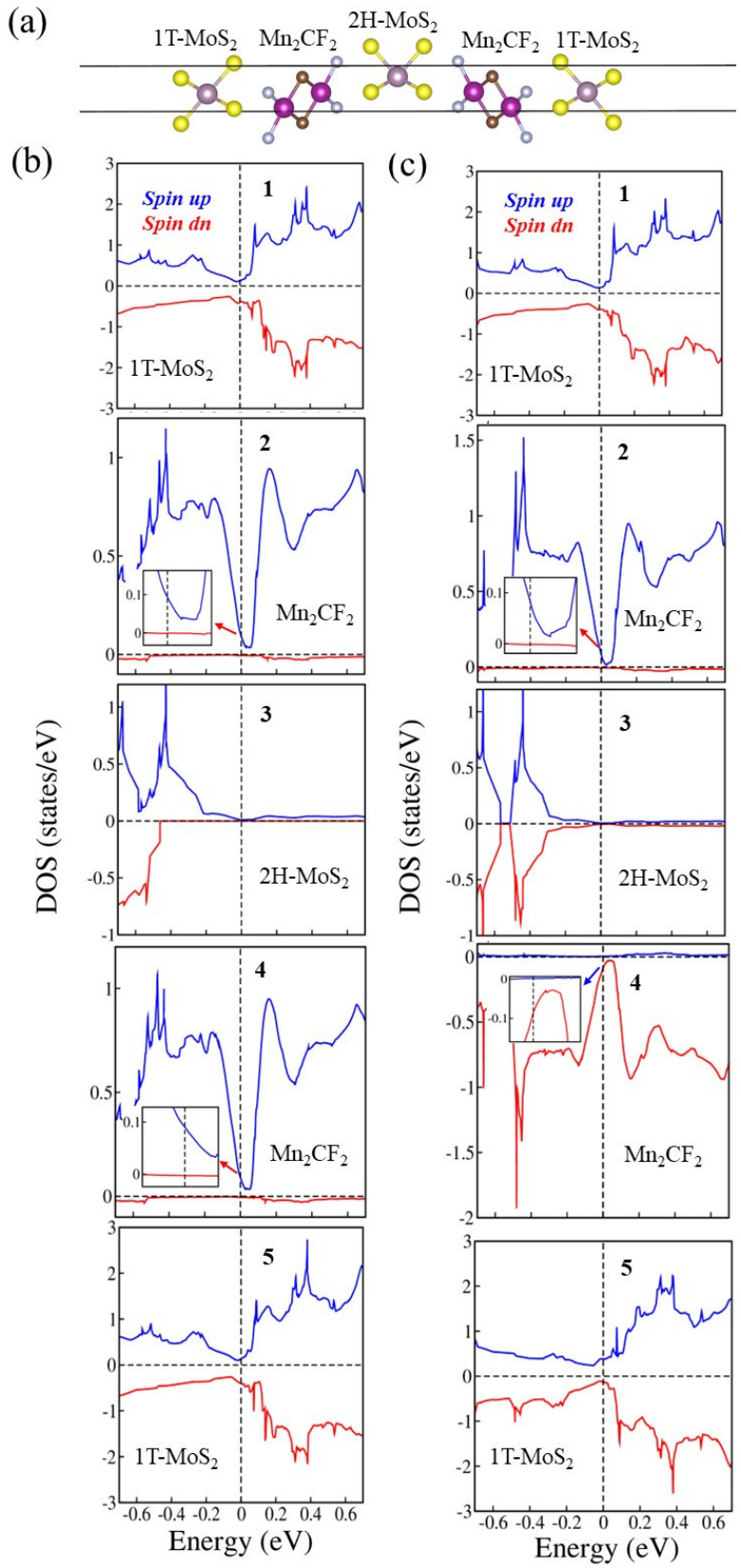

Figure S9: (a) Schematic illustration of the 1T-MoS_2/Mn_2CF_2/2H-MoS_2/Mn_2CF_2/1T-MoS_2 heterostructure. (b,c) Spin-resolved, layer-dependent density of states (DOS) in the energy window -0.7 to 0.7 eV for the parallel and antiparallel magnetic configurations, respectively. The insets show an enlarged view of the DOS near the Fermi level (E_F). The labels "1–5" denote the layer indices of the individual monolayers in the heterostructure.

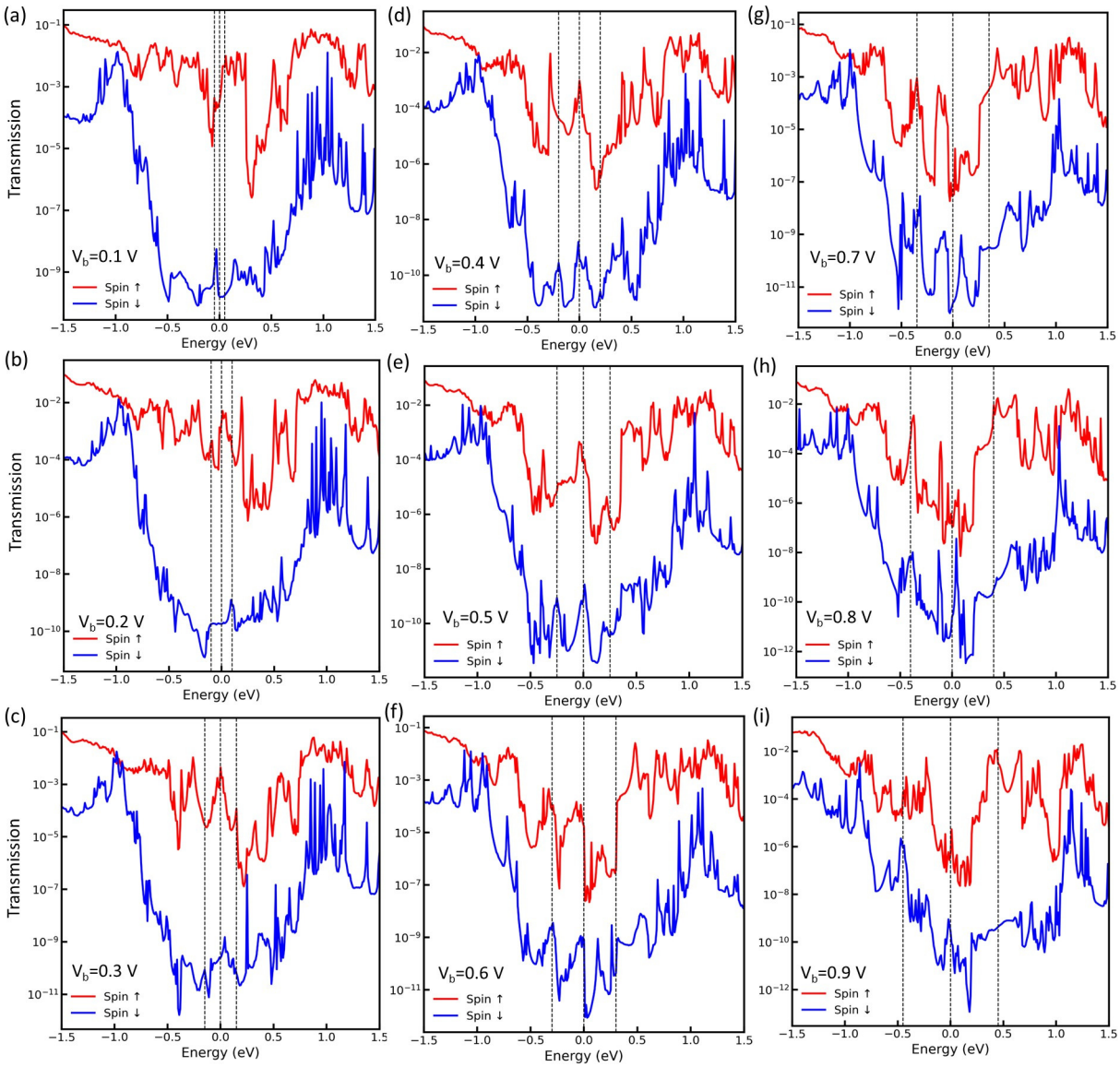

Figure S10: Bias-dependent transmission spectra as a function of energy in the parallel state for MTJ with a single layer of 2H-MoS_2 tunnel barrier (MTJ1).

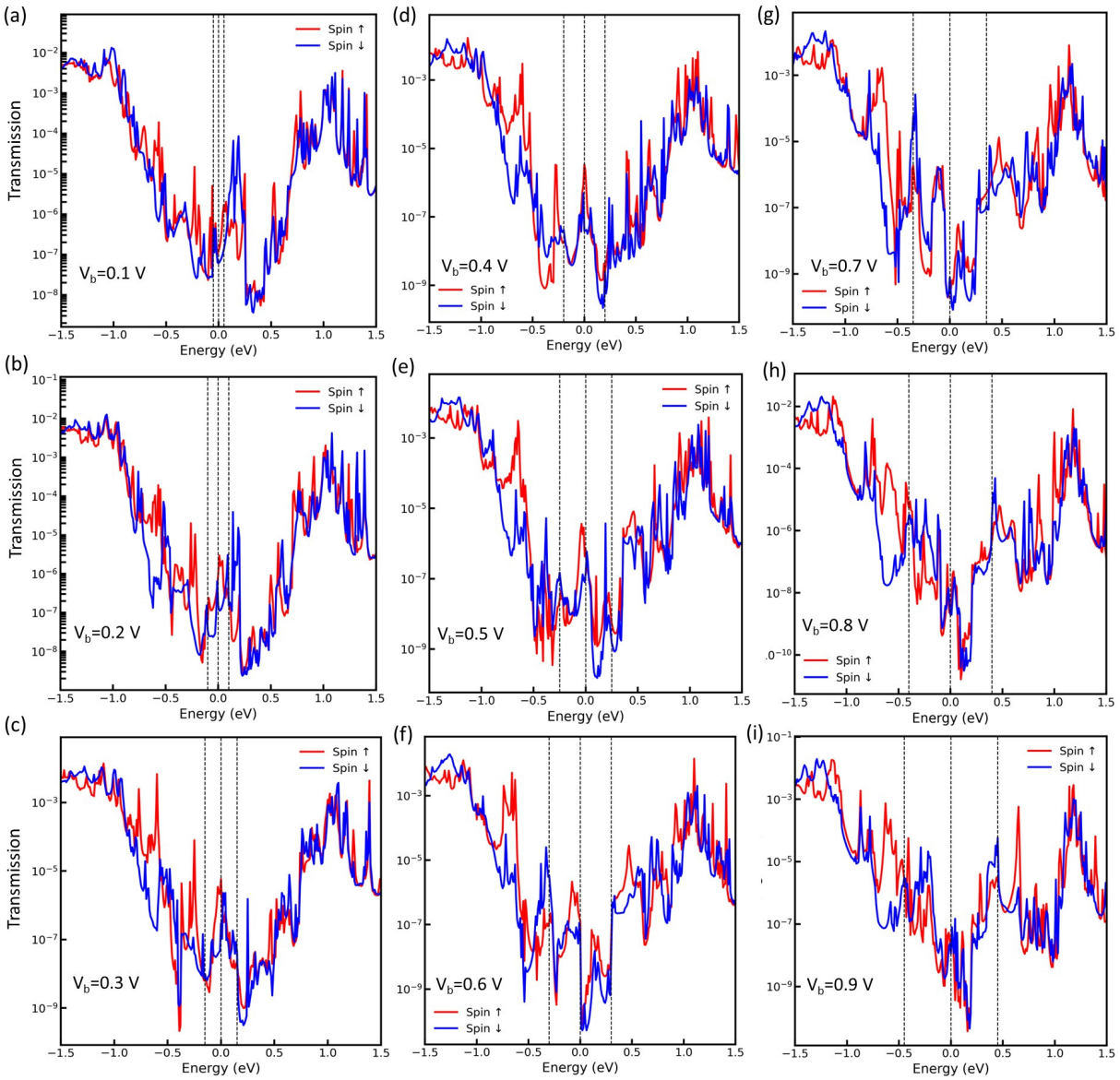

Figure S11: Bias-dependent transmission spectra as a function of energy in the antiparallel state for MTJ with a single layer of 2H-MoS_2 tunnel barrier (MTJ1).

5 Comprehensive Analysis of Nonmagnetic Barrier Variations in Magnetic Tunnel Junctions

Next, we analyzed MTJ, with a four-layer 2H-MoS2 barrier (MTJ2), exhibits strongly spin-polarized transport similar to MTJ1 (Fig. S12). At E_F, $T_{\mathrm{PC}}^{\uparrow}$ exceeds $T_{\mathrm{PC}}^{\downarrow}$ and $T_{\mathrm{APC}}^{\uparrow,\downarrow}$ by eight and three orders of magnitude, respectively, across a wide energy range, ensuring robust spin polarization and giant TMR. Spin-resolved I–V curves (Fig. S12(d–e)) show fully suppressed spin-down current and non-monotonic spin-up current with peaks near 0.2 V and 0.6 V, followed by a drop beyond 0.8 V, indicating NDR with a PVR of 49. Under applied bias voltage, spin-up transmission in the parallel state (Fig. S13) shifts to lower energies and exhibits oscillatory variations, while spin-down remains nearly constant; beyond 0.7 V, both both spin-up and spin-down channels are suppressed (Fig. S12(d)). In the antiparallel state (Fig.S14), bias-induced spin-channel segregation leads to non-monotonic currents that align with transmission peaks.

Similarly, the MTJ with a hybrid barrier consisting of single layers of both 1T- and 2H–MoS_2 (MTJ3), shows comparable spin-polarized transport to MTJ1 and MTJ2 (Fig. S15). At E_F, $T_{\mathrm{PC}}^{\uparrow}$ exceeds $T_{\mathrm{PC}}^{\downarrow}$ and $T_{\mathrm{APC}}^{\uparrow,\downarrow}$ by seven and four orders of magnitude across -0.4 to 0.4 eV, maintaining giant TMR and efficient spin filtering. The I–V curves (Fig. S15(d–e)) display fully suppressed spin-down current and non-monotonic spin-up current with peaks near 0.2 V and 0.7 V, indicative of NDR with a PVR of 25. Bias-dependent transmission Figs. S16–S17 shows that spin-up and spin-down channels conincides around 0.9 V, while in the antiparallel state, slight spin-channel separation produces non-monotonic current behavior consistent with the transmission profile.

Extending this trend, MTJ4 with a five layer–1T–MoS_2 barrier exhibits pronounced spin-polarized transport (Fig. S18(d–e)). At E_F, $T_{\mathrm{PC}}^{\uparrow}$ exceeds $T_{\mathrm{PC}}^{\downarrow}$ and $T_{\mathrm{APC}}^{\uparrow,\downarrow}$ by four and two orders of magnitude across -0.4 to 0.4 eV, maintaining a large TMR and strong spin selectivity. Under bias ($V_b = 0.1$–0.5 V), the spin-up current in the parallel state rises to ~ 0.3 V, decreases until ~ 0.5 V, and vanishes beyond this, while spin-down remains nearly constant (Fig. S18(d)), consistent with the transmission spectra (Fig. S19). Above 0.5 V, both spin channels converge, leading to vanishing current and loss of spin polarization. In the antiparallel state (Fig. S18(e)), spin channels remain distinct up to 0.5 V but merge at higher bias, resulting in equal transmission and nearly zero current.

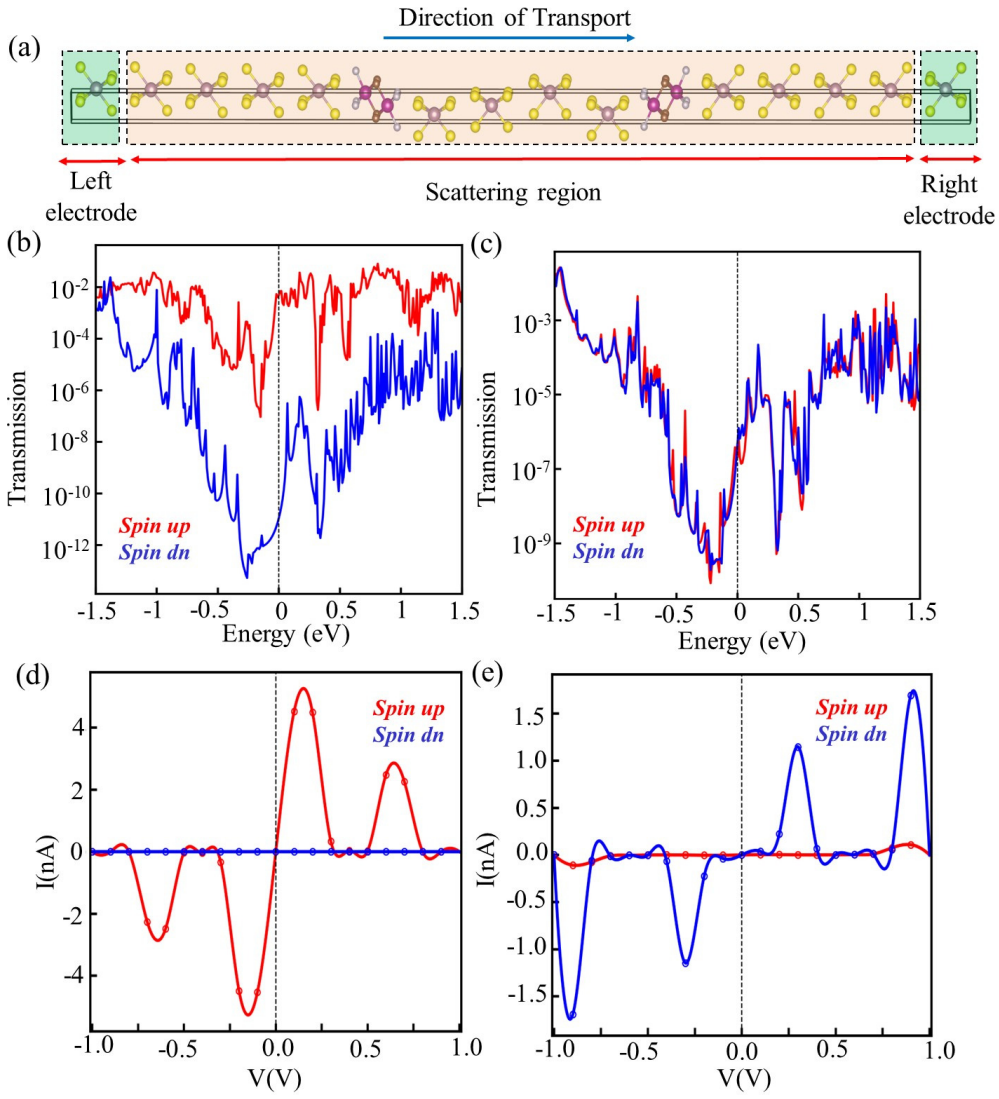

Figure S12: (a) Schematic illustration of the MTJ device with a four layer of 2H-MoS_2 tunnel barrier (MTJ2). (b, c) Spin-resolved transmission spectra of the parallel and antiparallel states, respectively, at zero bias. (d, e) Spin-resolved total currents in the parallel and antiparallel states, respectively, as functions of the bias voltage V.

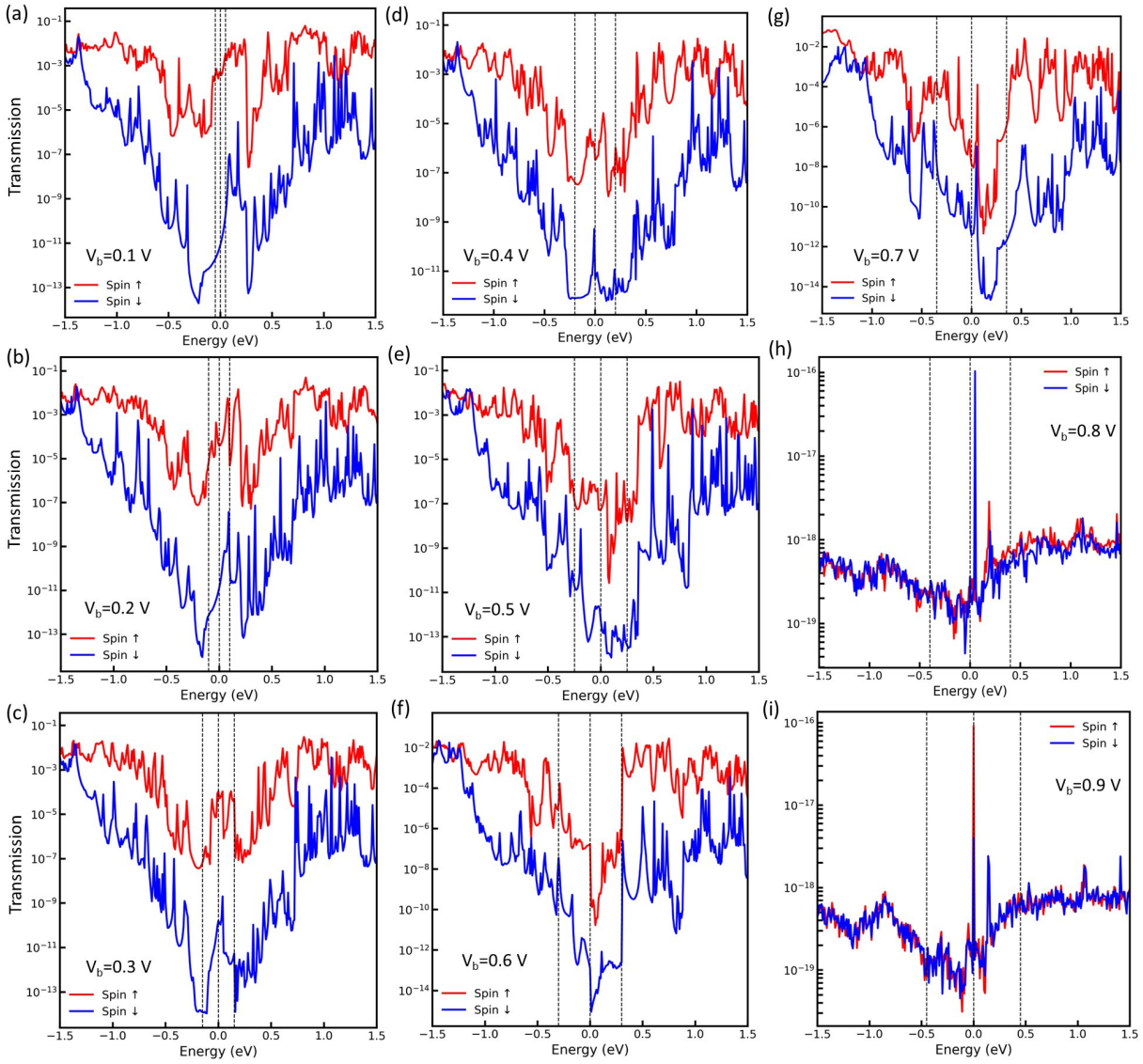

Figure S13: Bias-dependent transmission spectra as a function of energy in the parallel state for MTJ with a four layer of 2H-MoS_2 tunnel barrier (MTJ2).

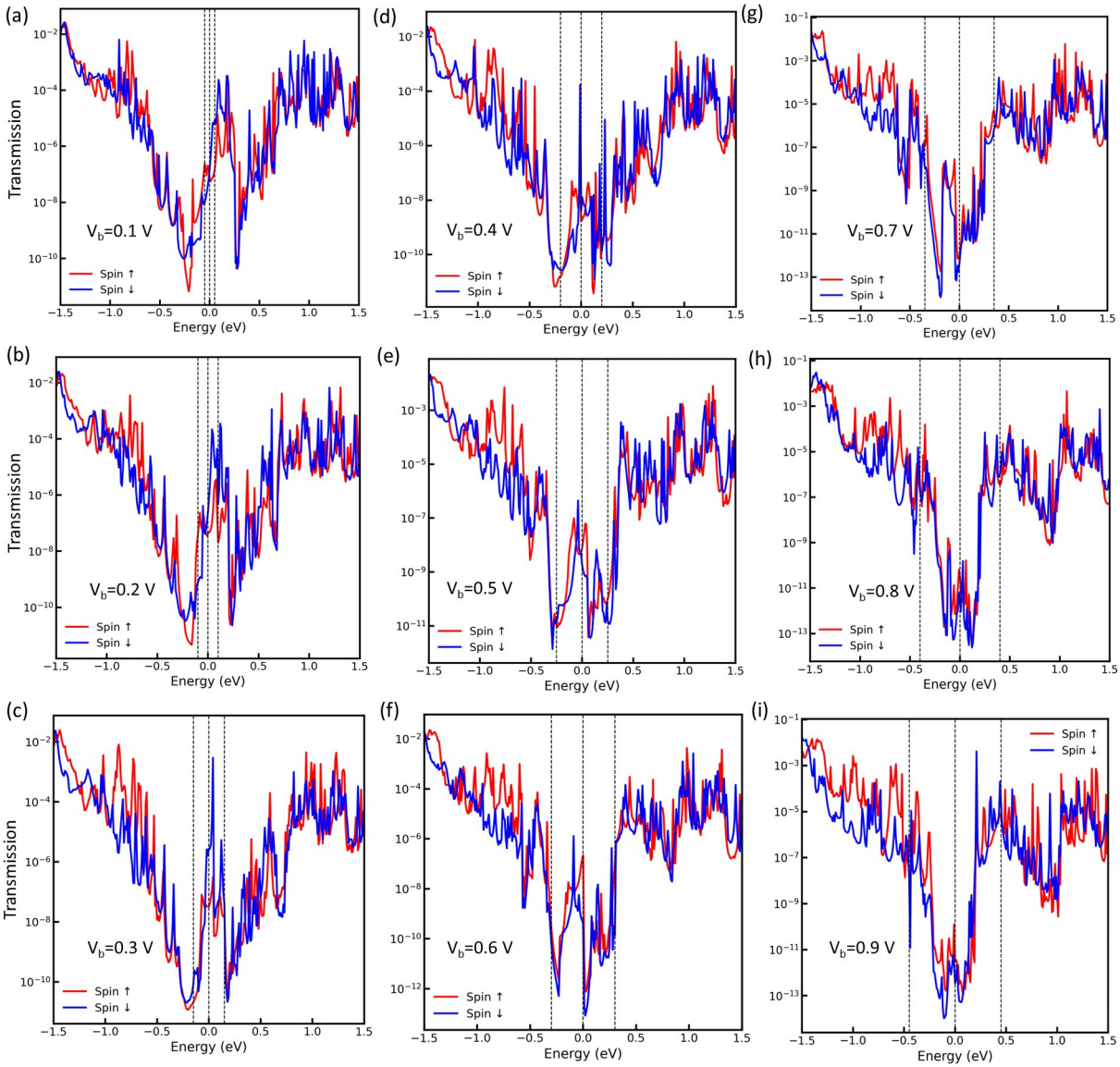

Figure S14: Bias-dependent transmission spectra as a function of energy in the antiparallel state for MTJ with a four layer of 2H-MoS_2 tunnel barrier (MTJ2).

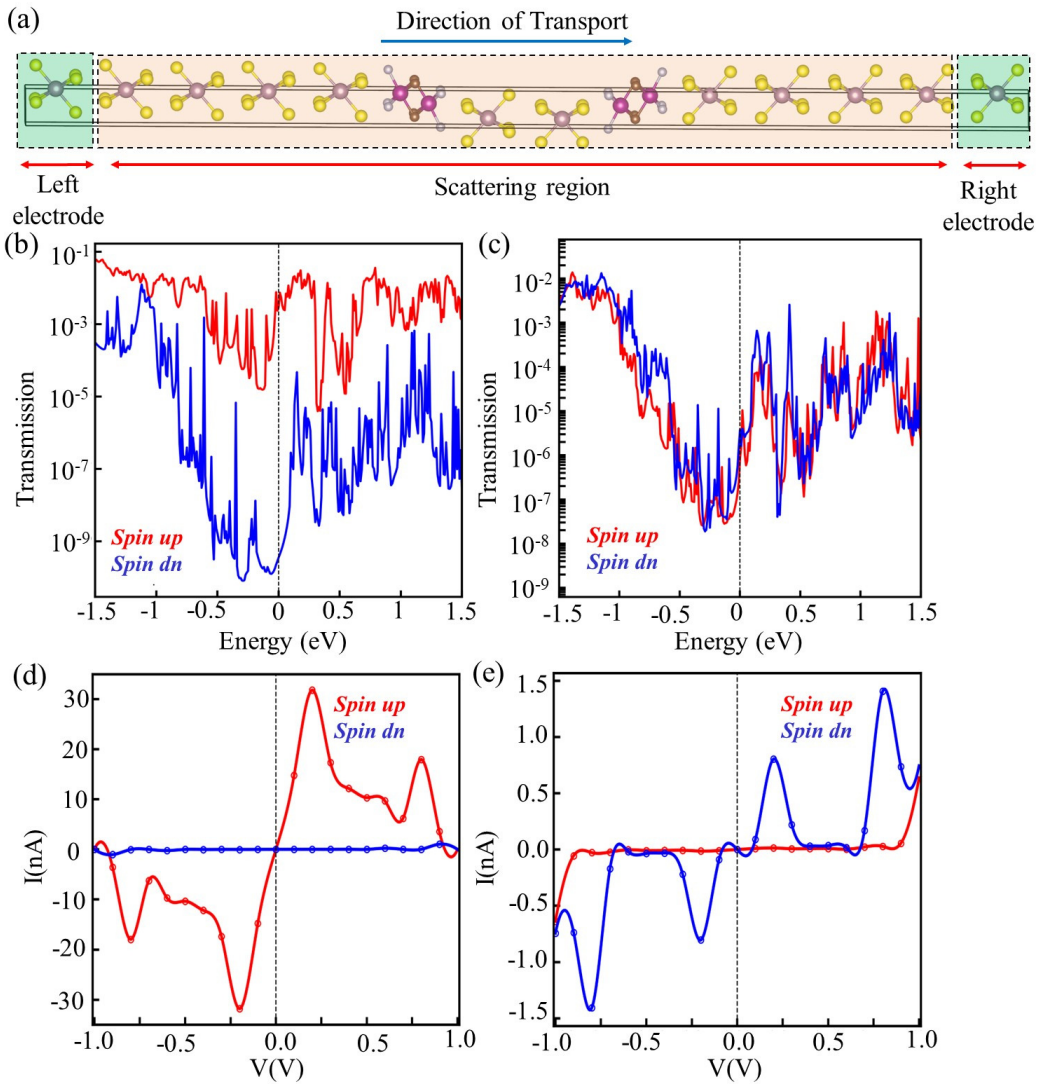

Figure S15: (a) Schematic illustration of the MTJ device with hybrid barrier consisting of single layers of both 1T- and 2H–MoS_2 (MTJ3). (b, c) Spin-resolved transmission spectra of the parallel and antiparallel states, respectively, at zero bias. (d, e) Spin-resolved total currents in the parallel and antiparallel states, respectively, as functions of the bias voltage V.

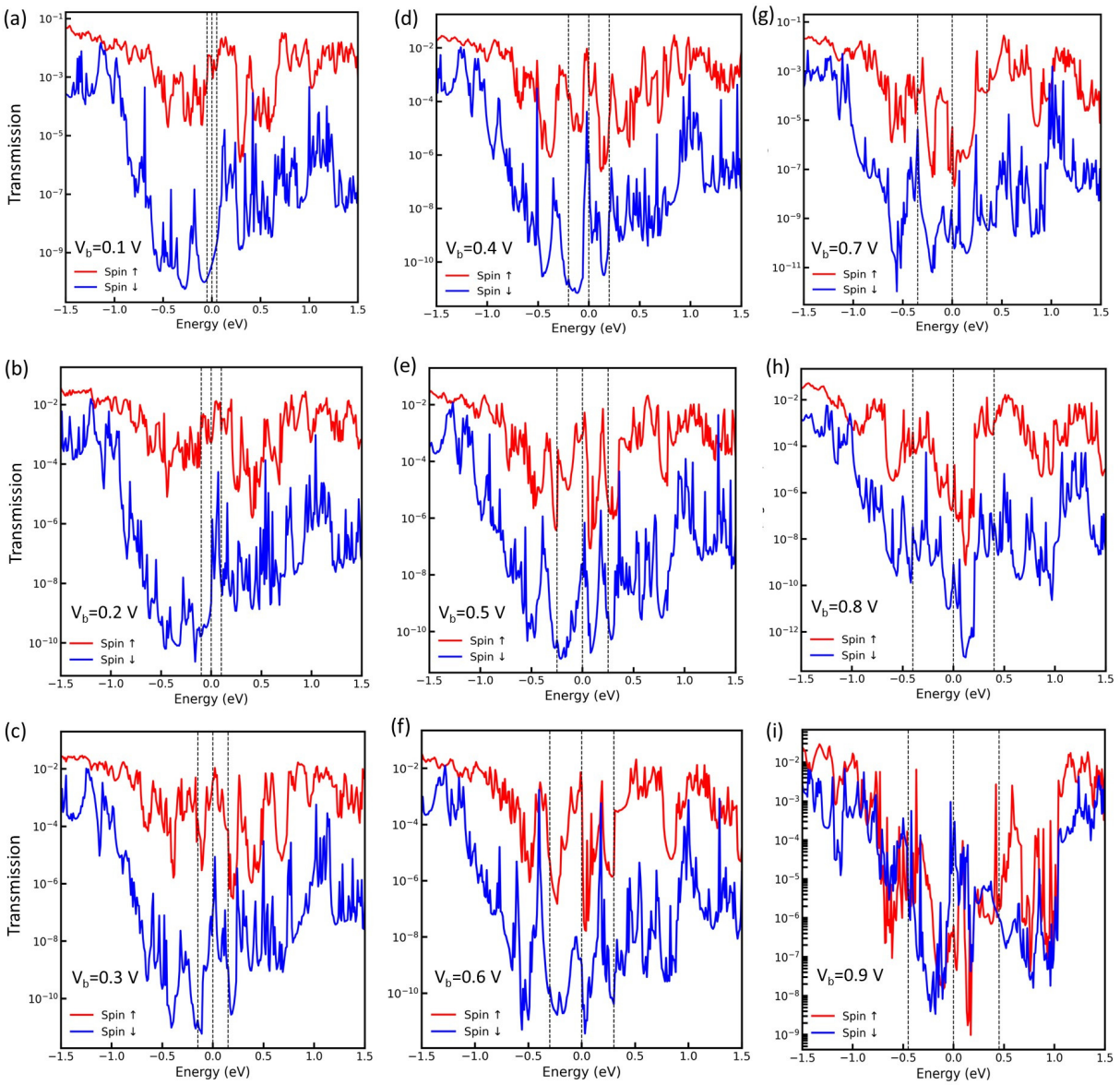

Figure S16: Bias-dependent transmission spectra as a function of energy in the parallel state for MTJ with hybrid barrier consisting of single layers of both 1T- and 2H–MoS_2 (MTJ3).

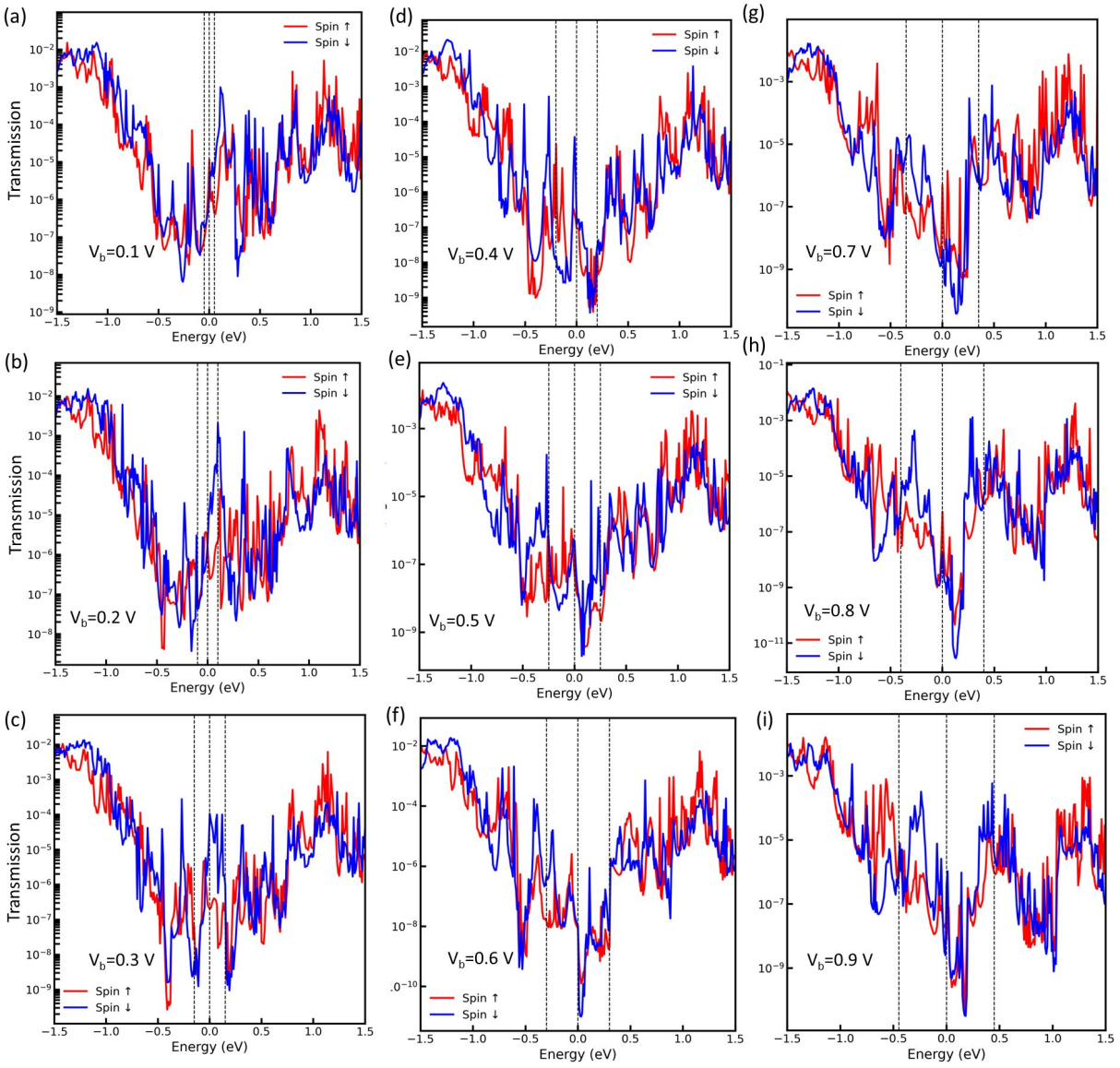

Figure S17: Bias-dependent transmission spectra as a function of energy in the antiparallel state for a hybrid barrier consisting of single layers of both 1T- and 2H–MoS_2 (MTJ3).

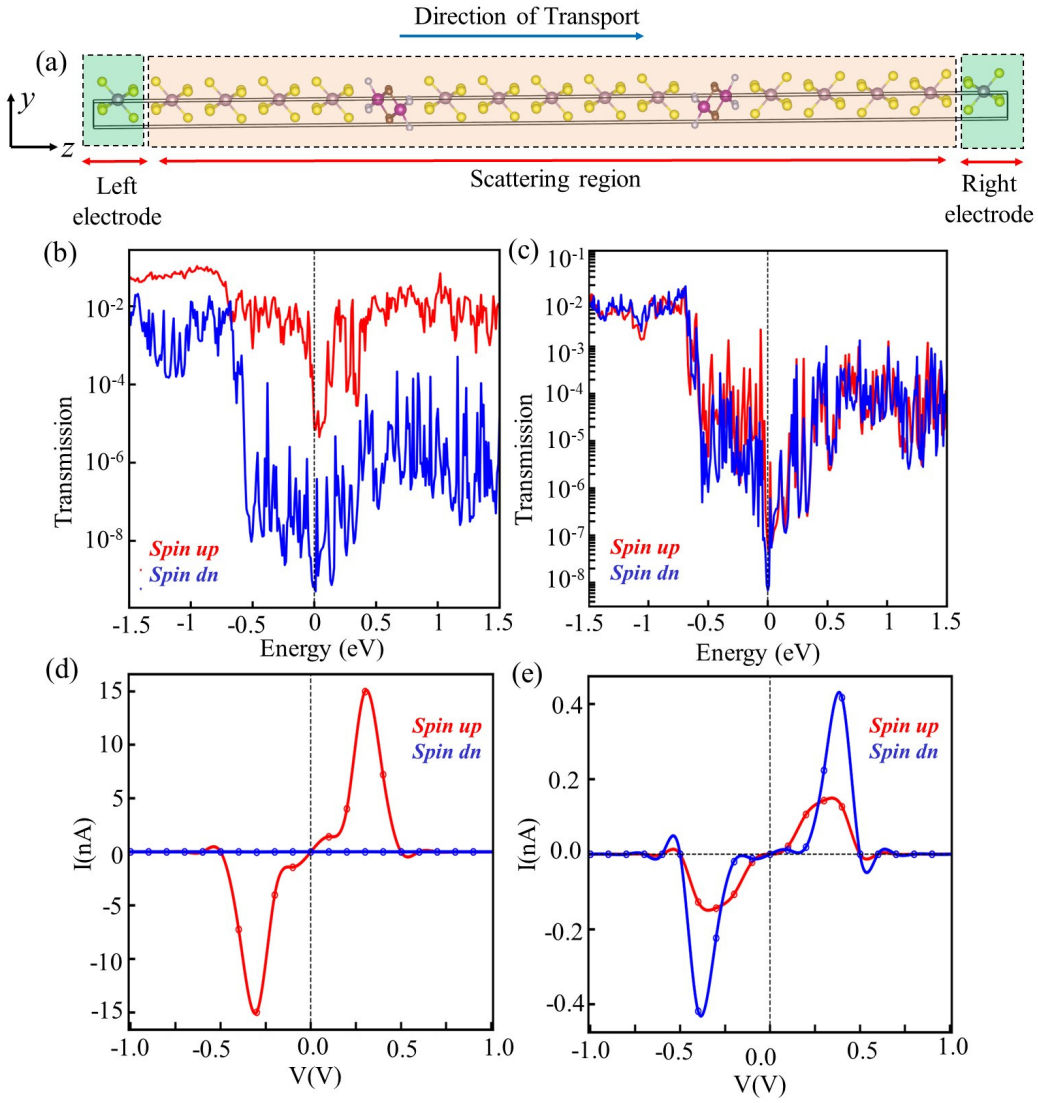

Figure S18: (a) Schematic illustration of the MTJ device with a five layer of 1T MoS_2 tunnel barrier (MTJ4). (b, c) Spin-resolved transmission spectra of the parallel and antiparallel states, respectively, at zero bias. (d, e) Spin-resolved total currents in the parallel and antiparallel states, respectively, as functions of the bias voltage V.

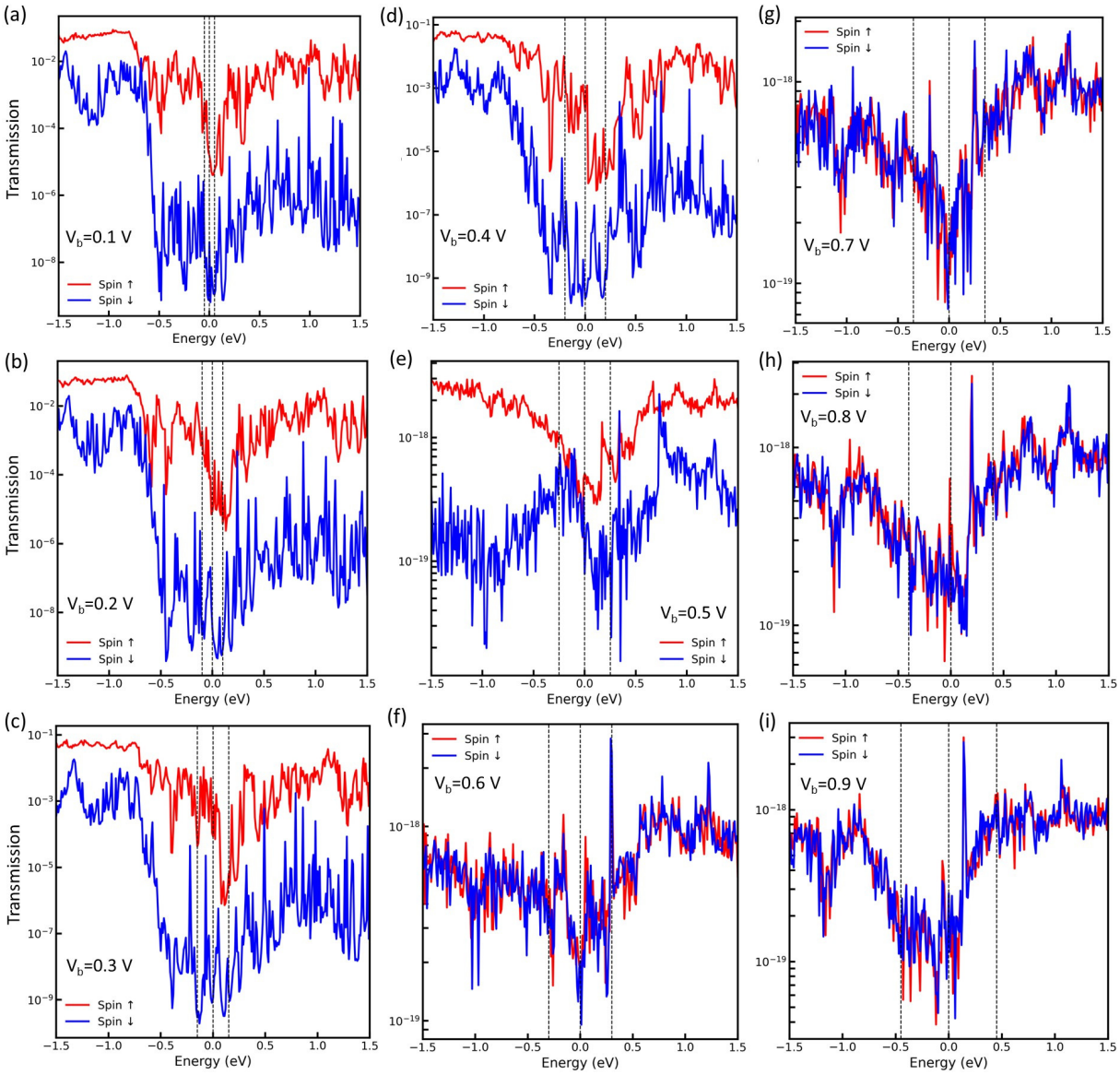

Figure S19: Bias-dependent transmission spectra as a function of energy in the parallel state of for MTJ with a five layer of 1T-MoS_2 tunnel barrier (MTJ4).

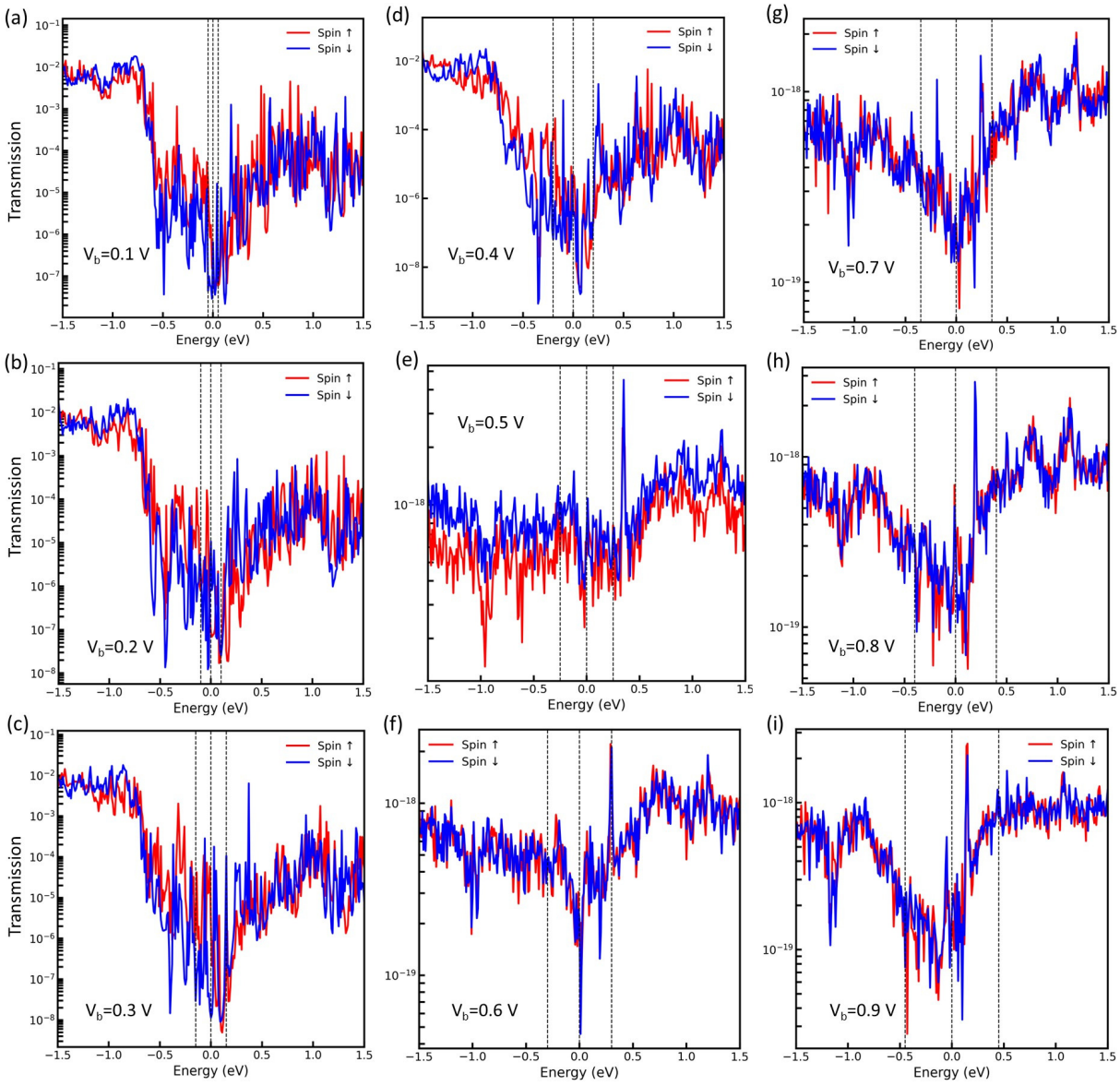

Figure S20: Bias-dependent transmission spectra as a function of energy in the antiparallel state for MTJ with a five layer of 1T-MoS_2 tunnel barrier (MTJ4).

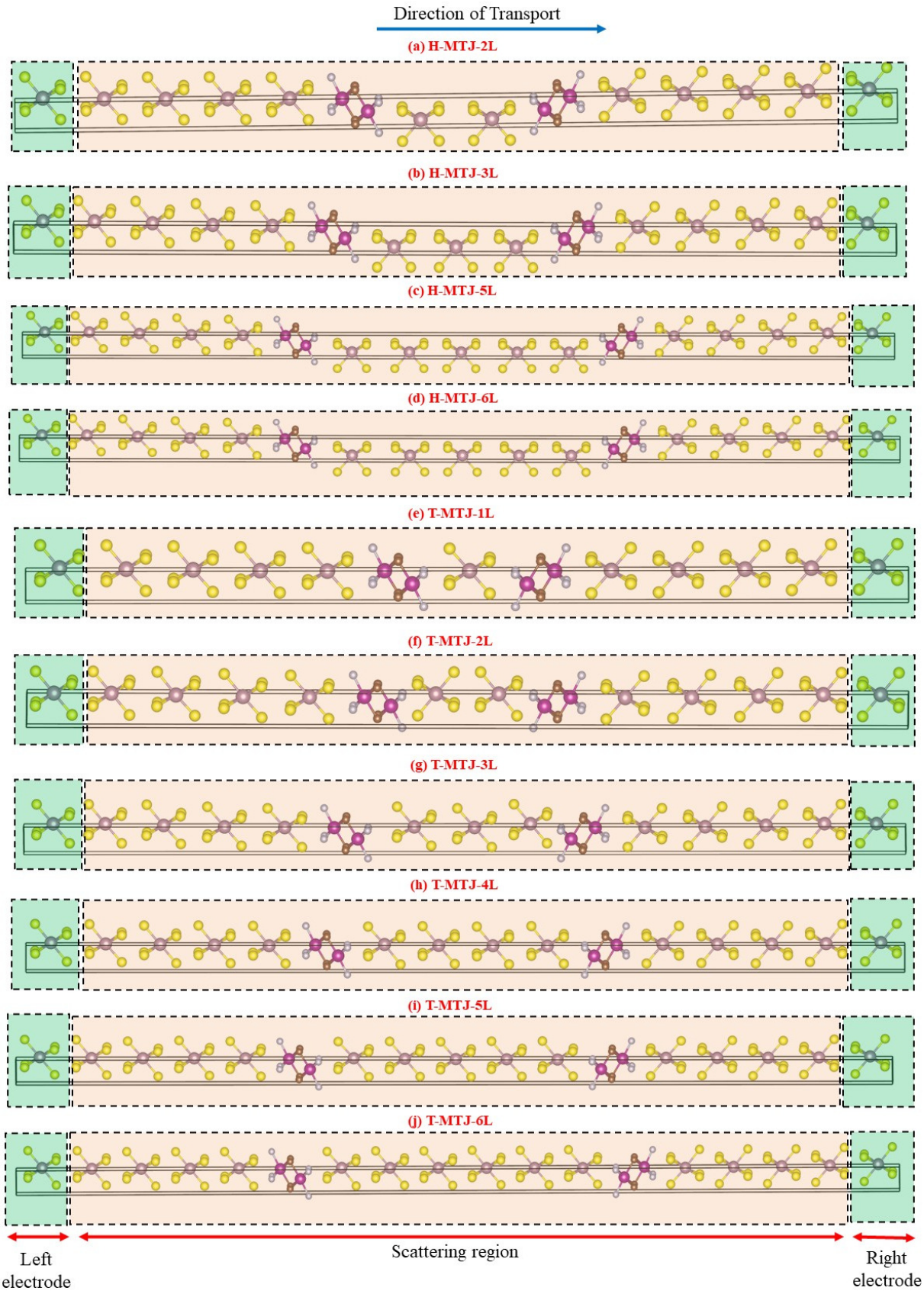

Figure S21: Schematic illustration of different device configurations: H-MTJ and T-MTJ, corresponding to homophase 2H–MoS_2 and homophase 1T–MoS_2 tunnel barriers, respectively. The notation 1L–6L denotes tunnel barriers consisting of one to six MoS_2 layers.

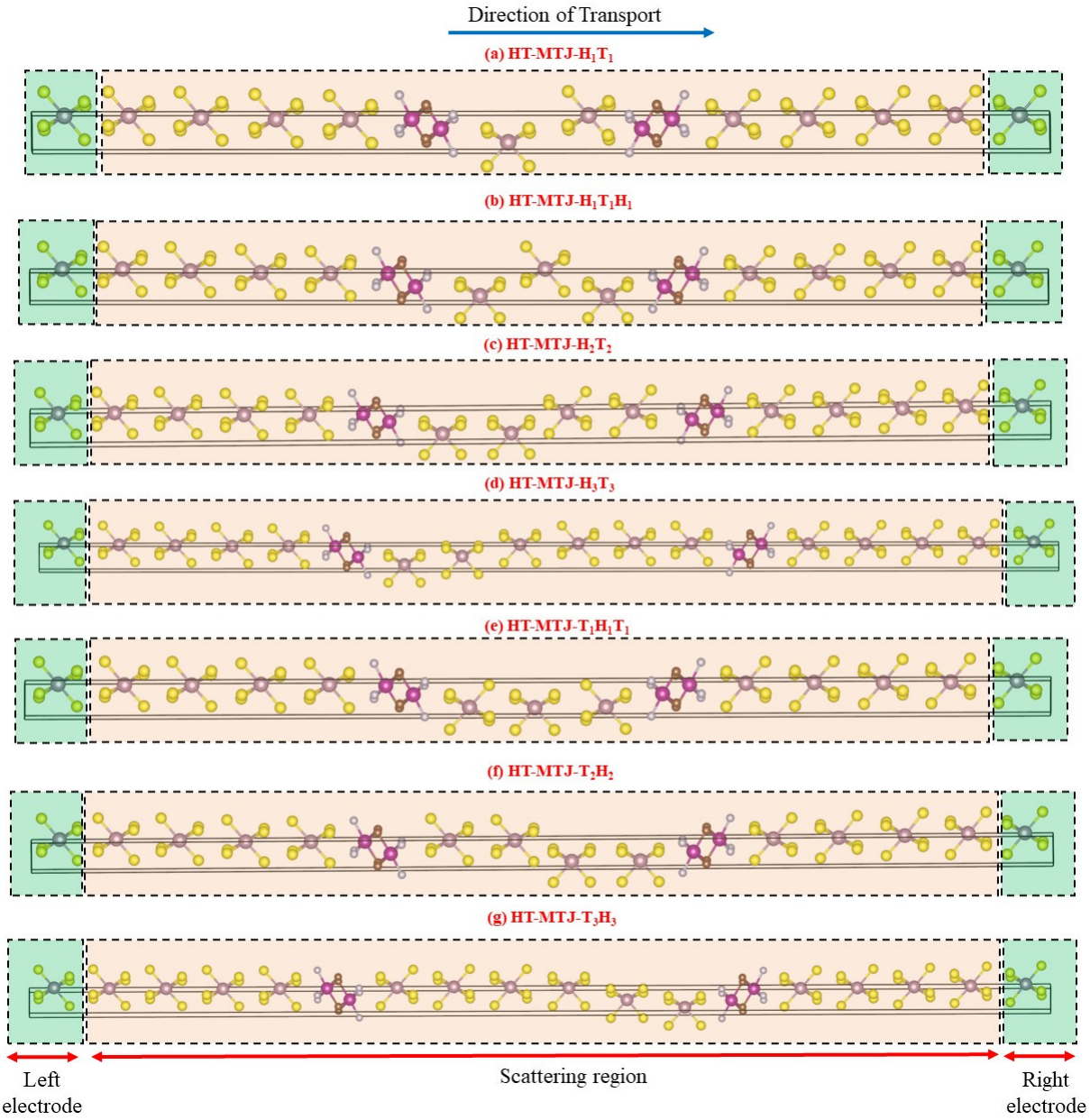

Figure S22: Schematic illustration of device configurations incorporating HT-MTJs, which denote heterophase (1T/2H) MoS_2 tunnel barriers. For HT-MTJ devices, the notation (H/T) represents the stacking sequence of 2H and 1T layers from left to right across the tunnel barrier, with numbers indicating multiple layers of each phase.

Table S2: Mulliken population analysis for the MTJ with a four-layer 2H-MoS_2 spacer. Spin-up and spin-down charges are given for each atom.

Atom Index	**Element**	**Spin-up Charge**	**Spin-down Charge**
Left Mn_2CF_2 Electrode			
15	F	3.678	3.688
16	Mn	5.620	0.896
17	C	1.380	2.791
18	Mn	5.628	0.921
19	F	3.679	3.693
Right Mn_2CF_2 Electrode			
32	F	3.680	3.693
33	Mn	5.628	0.921
34	C	1.379	2.791
35	Mn	5.620	0.897
36	F	3.678	3.688
MoS_2 Spacer/Barrier			
20	S	3.010	3.016
21	Mo	2.966	2.958
22	S	3.024	3.024
23	S	3.018	3.018
24	Mo	2.959	2.959
25	S	3.022	3.022
26	S	3.018	3.018
27	Mo	2.959	2.959
28	S	3.022	3.022
29	S	3.020	3.021
30	Mo	2.972	2.964
31	S	3.010	3.016

Table S3: Comparison of representative theoretical tunneling magnetoresistance (TMR) values reported for two-dimensional (2D) MXene- and van der Waals (vdW)–based magnetic tunnel junctions.

System	**Junction type**	**TMR (%)**	**Ref.**
$CrI_3/Ag/CrI_3$ (12 layers)	vdW MTJ	$> 10^9$	[1]
$CrI_3/WTe_2/CrI_3$	vdW MTJ	$\sim 10^5$	[2]
$CrI_3/Cr_2Ge_2Te_6$ (bilayer)	vdW MTJ	6.2×10^5	[3]
$CrSe_2/NiCl_2/CrSe_2$	vdW MTJ	1.2×10^4	[4]
$MnBi_2Te_4/BN/MnBi_2Te_4$	vdW MTJ	3.7×10^3	[5]
$CrPS_4$ (10 layers)	Spin-filter MTJ	3.7×10^5	[6]
Graphene/CrSBr/Graphene (4 layers)	Spin-filter MTJ	2×10^7	[7]
Fe_4GeTe_2 (layers)	vdW MTJ	~ 500	[8]
$Mn_2CF_2/Ti_2CO_2/Mn_2CF_2$	MXene-based MTJ	$\sim 10^6$	[9]
$ScCr_2C_2F_2$-based MTJ	MXene-based MTJ	$\sim 10^6$	[10]
$Sc_2CHO/Sc_2NHO/Sc_2CHO$	MXene-based MTJ	$\sim 2.5 \times 10^3$	[11]
This work	MXene/TMD vdW MTJ	$\mathbf{7.21 \times 10^5}$	**This work**

Table S4: Calculated magnetic moments (in μ_B) of Mn_1–Mn_4 atoms in the Mn_2CF_2 layers of MTJ4 under different applied electric fields. Negative values indicate spin-flip transitions.

Applied Field (V/Å)	**Mn_1**	**Mn_2**	**Mn_3**	**Mn_4**
-0.40	-2.45	-4.27	-2.70	-4.24
-0.30	3.28	3.07	2.65	-2.65
-0.20	4.29	4.29	4.27	4.27
-0.10	4.27	4.29	4.28	4.28
0.00	4.28	4.29	4.28	4.29
0.10	4.28	4.27	4.29	4.28
0.20	4.29	4.29	4.29	4.30
0.30	0.48	4.29	4.23	2.70
0.40	4.28	-1.80	-2.56	-2.35

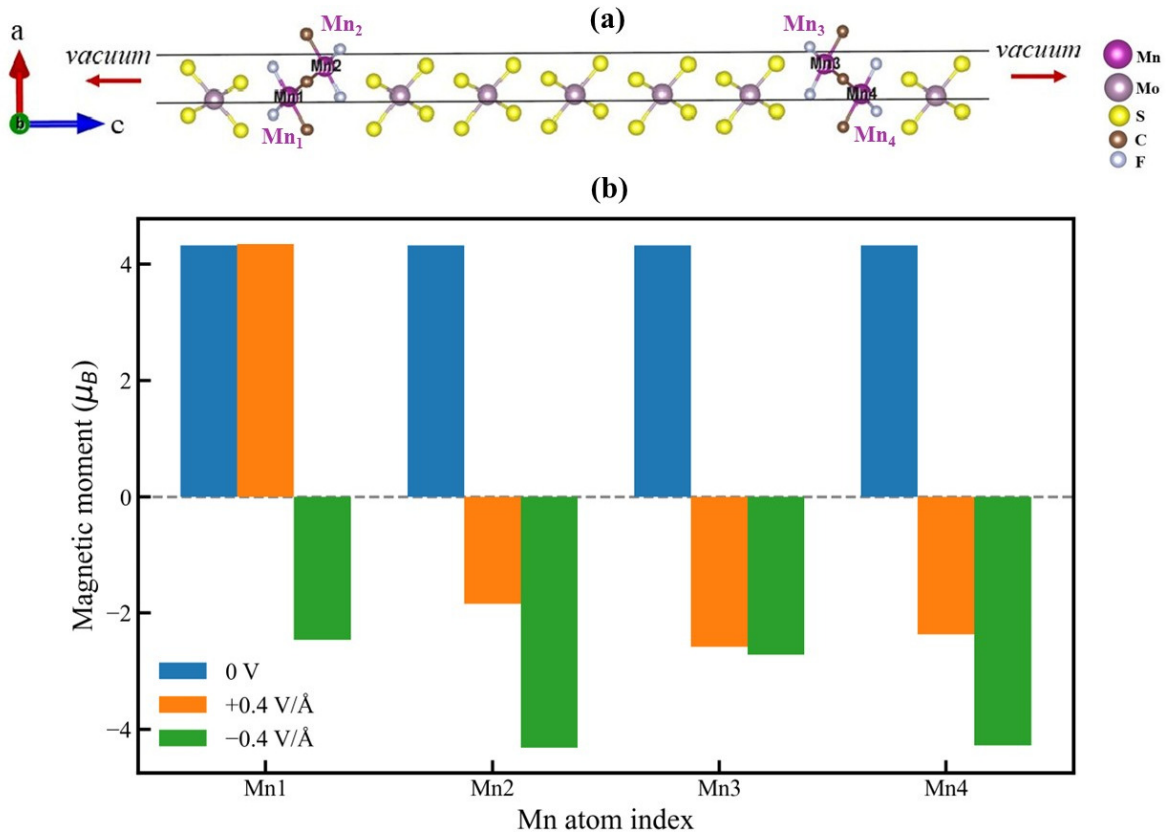

Figure S23: (a) Schematic illustration of the 1T-MoS_2/Mn_2CF_2/5L-1T-MoS_2/Mn_2CF_2/1T-MoS_2 heterostructure. The corresponding Mn atoms are labeled as Mn_1–Mn_4. (b) Electric-field-induced variation of the Mn atomic magnetic moments.

Table S5: Variation of exchange energy, $E_{ex} = E_{AFM} - E_{FM}$ (in eV), of MTJ4 under different applied electric fields.

Applied Field (V/Å)	E_{ex} **(eV)**
-0.40	-4.87
-0.30	-1.15
-0.20	1.75
-0.10	0.88
0.00	0.007
0.01	0.023
0.20	0.04
0.30	-1.36
0.40	-3.46

Table S6: Spin-dependent transmission coefficients at the Fermi level and corresponding TMR values for MTJ2 (four-layer barrier) calculated with different DFT+U values.

Device	U **(eV)**	$T_{\mathrm{PC}}(E_F)$	$T_{\mathrm{APC}}(E_F)$	**TMR (%)**
H-MTJ-4L (MTJ2)	3	8.31×10^{-4}	2.33×10^{-7}	3.57×10^{5}
H-MTJ-4L (MTJ2)	4	4.99×10^{-3}	6.92×10^{-7}	7.21×10^{5}
H-MTJ-4L (MTJ2)	5	5.05×10^{-4}	8.15×10^{-8}	6.20×10^{5}

6 Variation of TMR with different DFT+U values

As shown in Table S6, although the absolute values of the spin-dependent transmission coefficients and the resulting TMR vary slightly with the Hubbard parameter U, the overall transport behavior remains unchanged. In particular, the transmission in the parallel configuration remains several orders of magnitude larger than that in the antiparallel configuration, leading to robust spin-filtering and large TMR values. The robustness observed for this representative junction is expected to extend to the other MTJ configurations because the tunneling mechanism in all devices is governed by the same intrinsic property of the Mn_2CF_2 spin-filter barrier, namely its half-metallic electronic structure and nearly perfect spin polarization. Moreover, the half-metallic gap of Mn_2CF_2 is preserved for $U = 3$ and $U = 5$ eV (see Fig. S3), demonstrating that moderate variations of U mainly affect the half-metallic gap and the quantitative magnitude of the exchange splitting but do not alter the underlying spin-selective tunneling mechanism. Consistently, nearly perfect spin polarization is obtained for all MTJs (see Table 1 of the manuscript) for $U = 4$ eV, where the transmission in the parallel configuration remains two to three orders of magnitude larger than that in the antiparallel configuration, leading to strong spin-filtering behavior and large TMR values. Since all MTJs employ the same electrodes and spin-filter barrier and differ only in stacking or barrier thickness, the qualitative transport behavior and the relative trends in TMR observed for $U = 4$ are expected to remain largely unchanged for $U = 3$ and $U = 5$ eV.

7 Electric field induced spin flip

To elucidate the microscopic mechanism underlying the electric-field-driven magnetic transition in MTJ4, we analyzed the total and Mn atomic-projected density of states (DOS), as shown in Fig. S24. At zero electric field [Fig. S24(d)], the Mn states exhibit a pronounced spin asymmetry near the Fermi level, reflecting strong exchange splitting

and a robust half-metallic character of the Mn_2CF_2 spin-filter barrier. Consequently, only one spin channel contributes at E_F, resulting in nearly 100% spin polarization and a stable ferromagnetic ground state. Upon applying a finite electric field of ± 0.4 V/Å [Fig. S24(e,f)], the Mn projected DOS undergoes a substantial reconstruction: minority-spin states shift toward and cross E_F, destroying the half-metallic character and giving rise to finite DOS contributions from both spin channels at the Fermi level. As a result, the spin polarization is strongly reduced, consistent with the behavior observed beyond the critical bias of ~ 0.4 V in Fig. 6(h) of the manuscript.

Furthermore, with increasing electric field (particularly at ± 0.4 V/Å), the total DOS [Fig. S24(b,c)] shows that the electronic states near E_F shift toward lower energies, leading to a slight reduction of the spin-up DOS at the Fermi level. In addition, the spin-up DOS peak approaches and crosses E_F, accompanied by a redistribution of spectral weight between the spin-up and spin-down states. As a consequence, the total DOS becomes nearly spin symmetric, closely resembling an antiferromagnetic electronic structure. This systematic reduction of spin asymmetry signifies a pronounced weakening of the exchange splitting within the Mn_2CF_2 layer, driven by electric-field-induced charge redistribution and enhanced interfacial hybridization with the metallic 1T–MoS_2 barrier. Overall, the polarity-dependent and continuous evolution of the DOS confirms that the observed spin-flip transition originates from an electric-field- controlled modification of magnetic exchange energies, ultimately stabilizing an antiferromagnetic configuration and leading to the reduction of spin polarization and tunneling magnetoresistance beyond the critical bias of ~ 0.4 V.

A detailed calculation of individual exchange interaction parameters (such as J_1 and J_2) is beyond the scope of the present work and will be addressed in future studies. Nevertheless, electric-field-controlled magnetic transitions of this type are well established in the literature. Such electric-field-controlled magnetic transitions are well established in the literature. For example, Sahoo *et al.* demonstrated electric-field-induced switching between ferromagnetic and antiferromagnetic states in Mn dimer, where charge transfer and interfacial hybridization modify the exchange interaction and even activate double-exchange mechanisms [12]. Similarly, electric-field-driven spin flipping and suppression of TMR have been reported in graphene and h-BN-based magnetic tunnel junctions, where field-induced redistribution of spin-resolved density of states at the interface governs the magnetic alignment and transport response [13]. More recently, Gogoi and Deb showed that electric fields can induce layer-selective spin flipping and exchange sign reversal in Janus van der Waals magnets, explicitly linking the phenomenon to field-driven charge redistribution and interfacial screening effects [14].

In MTJ4, stabilization of the antiferromagnetic configuration under strong electric fields

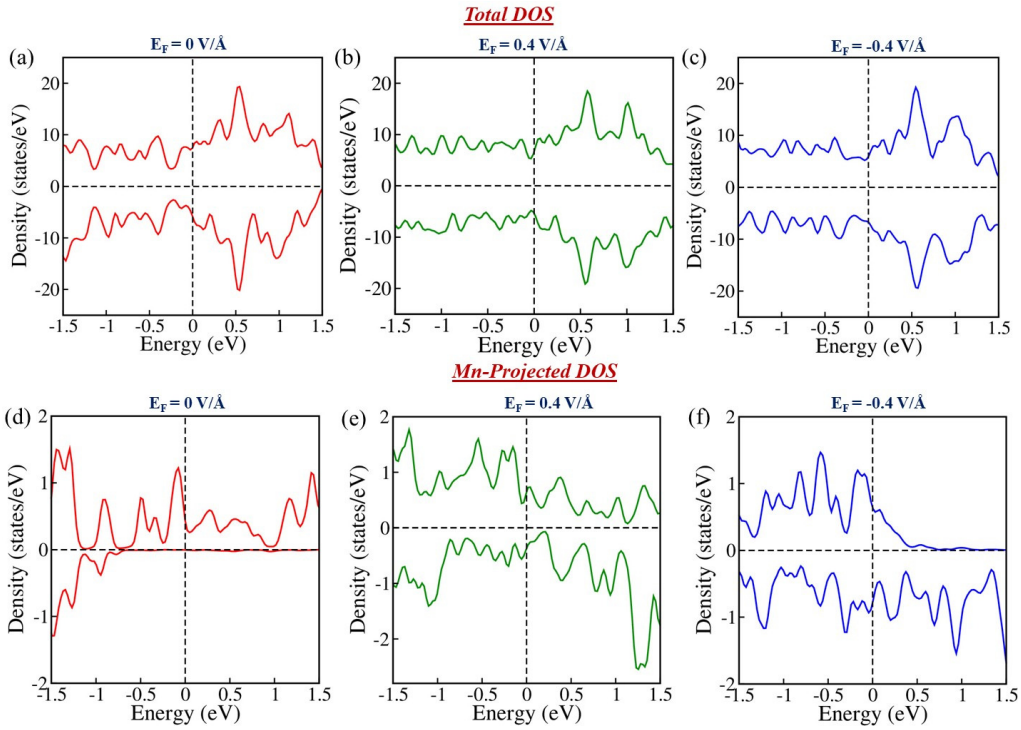

Figure S24: (a–c) Spin-polarized total local density of states at zero electric field and under applied electric fields of +0.4 and −0.4 V/Å. (d–e) Corresponding Mn atomic projected density of states under the same electric-field conditions.

naturally explains the simultaneous suppression of both spin-up and spin-down currents and the near-zero spin injection efficiency. Once the AFM state is stabilized, the spin-resolved transmission becomes nearly symmetric, spin filtering is lost, and the tunneling magnetoresistance collapses, as discussed in the manuscript and shown in Fig. S19.

Table S7: Calculated transmission coefficients at the Fermi level for different tunnel barriers in the parallel configuration (PC), $T_{\mathrm{PC}}(E_f)$, and antiparallel configuration (APC) with SOC, $T_{\mathrm{APC}}(E_f)$, along with the corresponding TMR ratios for various MTJ devices.

Device	$T_{\mathrm{PC}}(E_f)$	$T_{\mathrm{APC}}(E_f)$	**TMR (%)**
H-MTJ-1L (MTJ1)	6.74×10^{-5}	3.27×10^{-7}	2.05×10^{4}
H-MTJ-4L (MTJ2)	1.11×10^{-7}	3.63×10^{-9}	2.95×10^{3}
HT-MTJ-T1 H1 (MTJ3)	5.89×10^{-6}	1.94×10^{-7}	2.92×10^{3}
T-MTJ-5L (MTJ4)	2.35×10^{-2}	2.49×10^{-5}	9.41×10^{4}

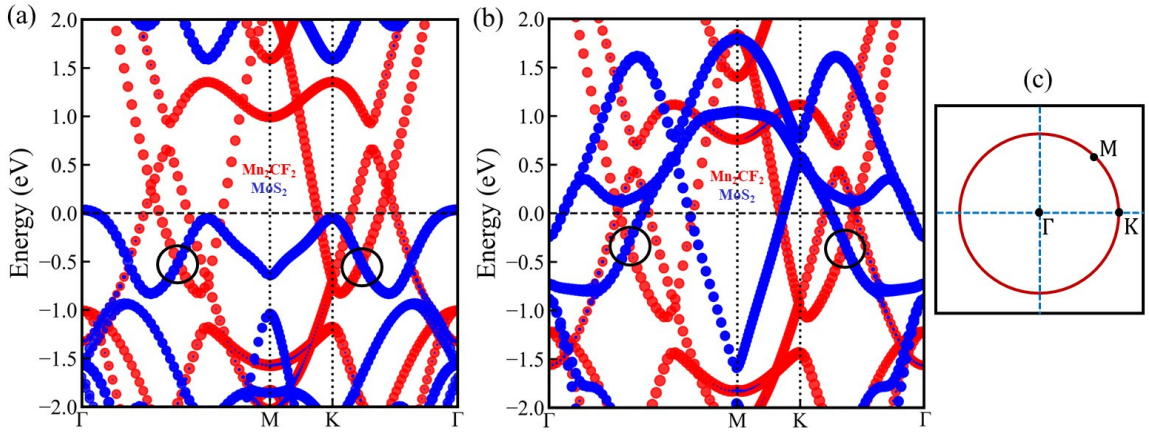

Figure S25: Projected band structures of (a) 2H-MoS_2/Mn_2CF_2 and (b) 1T-MoS_2/Mn_2CF_2 heterostructures, with the black circles highlighting the band crossing points. (c) Schematic illustration of the nodal ring formation in the 2D Brillouin zone.

7.1 Topological Aspects

Although the topological properties of monolayer Mn_2CF_2 have not yet been investigated, and 1T-MoS_2 itself is topologically trivial, the formation of the 1T-MoS_2/Mn_2CF_2 heterostructure gives rise to interesting band-crossing features along the high-symmetry paths Γ–M and K–Γ as shown in Fig. S25(b). These crossings may potentially evolve into nodal-line or nodal-ring-like features near the Fermi level. Similarly, the 2H-MoS_2 barrier also exhibits band crossings along the same symmetry directions, which can host nodal-line states protected by the mirror symmetry M_z Fig. S25(a).

Although the present study does not focus on the topological characterization of the heterostructure, it is worth noting that the interfacial coupling can induce symmetry breaking or preservation depending on the stacking configuration. Such symmetry modifications may give rise to nontrivial topological phases, motivating future investigations into the detailed topological electronic structure and their implications for spintronic applications.

References

[1] B. Wu, J. Yang, R. Quhe, S. Liu, C. Yang, Q. Li, *et al.*, Phys. Rev. Appl. **17**, 034030 (2022), doi:10.1103/PhysRevApplied.17.034030.

[2] N. Pandey and O. Grånäs, ACS Appl. Mater. Interfaces **17**, 51448–51456 (2025), doi:10.1021/acsami.5c10764.

[3] B. Liu, X. X. Ren, X. Zhang, P. Li, Y. Dong, and Z. X. Guo, "Electric field tunable multi-state tunnel magnetoresistances in 2D van der Waals magnetic heterojunctions," *Appl. Phys. Lett.* **122**, 151601 (2023). https://doi.org/10.1063/5.0139076

[4] X. Guo, Y. Zhu, B. Yang, X. Zhang, X. Han, and Y. Yan, "Large tunneling magnetoresistance and low resistance-area product in $CrSe_2/NiCl_2/CrSe_2$ van der Waals magnetic tunnel junction," *Appl. Phys. Lett.* **121**, 041601 (2022). https://doi.org/10.1063/5.0098687

[5] L. Zhang, H. Li, Y. Jiang, Z. Wang, T. Li, and S. Ghosh, "Current-driven magnetoresistance in van der Waals spin-filter antiferromagnetic tunnel junctions with $MnBi_2Te_4$," *Phys. Rev. Appl.* **20**, 044056 (2023). https://doi.org/10.1103/PhysRevApplied.20.044056

[6] J. Yang, S. Fang, Y. Peng, S. Liu, B. Wu, R. Quhe, ... and J. Yang, "Layer-Dependent Giant Magnetoresistance in Two-Dimensional $CrPS_4$ Magnetic Tunnel Junctions," *Phys. Rev. Appl.* **16**, 024011 (2021). https://doi.org/10.1103/PhysRevApplied.16.024011

[7] H. Liu, Y. Y. Liu, H. Wen, H. Wu, Y. Zong, J. Xia, and Z. Wei, "Spin-filter magnetic tunnel junctions based on A-type antiferromagnetic CrSBr with giant tunnel magnetoresistance," *Magnetochemistry* **8**, 89 (2022). https://doi.org/10.3390/magnetochemistry8080089

[8] A. Halder, D. Nell, A. Sihi, A. Bajaj, S. Sanvito, and A. Droghetti, "Half-metallic transport and spin-polarized tunneling through the van der Waals ferromagnet Fe_4GeTe_2," *Nano Lett.* **24**, 9221–9228 (2024). https://doi.org/10.1021/acs.nanolett.4c01479

[9] E. Balcı, U. O. Akkus, and S. Berber, ACS Appl. Mater. Interfaces **11**, 3609–3616 (2018), doi:10.1021/acsami.8b20202.

[10] Z. Cui, Y. Zhang, R. Xiong, C. Wen, J. Zhou, B. Sa, and Z. Sun, Giant tunneling magnetoresistance in two-dimensional magnetic tunnel junctions based on double transition-metal MXene $ScCr_2C_2F_2$, *Nanoscale Adv.* **4**, 5144–5153 (2022), doi:10.1039/D2NA00623E.

[11] B. Liu, S. Zhu, T. Wang, and S. Liu, "MXene-based $Sc_2CHO/Sc_2NHO/Sc_2CHO$ magnetic tunnel junctions for multi-value logic computing devices: A first-principles study," *ACS Applied Nano Materials* **6**(7), 5853–5859 (2023). DOI: 10.1021/acsanm.3c00240.

[12] M. R. Sahoo, S. K. Nayak, and K. Pradhan, J. Phys. Chem. C **126**, 4638–4646 (2022), doi:10.1021/acs.jpcc.1c10245.

[13] M. R. Sahoo, A. K. Kushwaha, R. Pati, P. M. Ajayan, and S. K. Nayak, J. Magn. Magn. Mater. **484**, 462–471 (2019), doi:10.1016/j.jmmm.2019.03.112.

[14] L. Gogoi and P. Deb, Phys. Rev. B **109**, 174439 (2024), doi:10.1103/PhysRevB.109.174439.